

# Evaluation of Photoacoustic Transduction Efficiency of Candle Soot Nanocomposite Transmitters

Wei-Yi Chang , Xu A. Zhang, Jinwook Kim, Wenbin Huang, Abhijeet Bagal, Chih-Hao Chang, Tiegang Fang , Hanchang Felix Wu, and Xiaoning Jiang 

**Abstract**—Candle soot nanoparticles (CSNP) and polydimethylsiloxane (PDMS) composite has shown the highly efficient photoacoustic transduction owing to their high light absorption coefficient and low interfacial thermal resistance. In this study, we report the effect of candle soot structure and thickness on the photoacoustic transduction efficiency. Optical properties of the CSNP/PDMS nanocomposites were characterized through both experimental measurements and finite difference time domain analysis in the visible wavelength range, indicating that the carbon volume fraction and thickness of CS/PDMS composite are highly relevant with light absorption. With a low laser energy input ( $<1$  mJ/pulse), the CS/PDMS composite with  $2.15 \mu\text{m}$  thickness exerts an output pressure of 3.78 MPa and a conversion efficiency of  $9.69 \times 10^{-3}$ , which is two orders of magnitude higher than previously reported results.

**Index Terms**—Photoacoustic efficiency, FDTD simulation, candle soot, carbon nanoparticles, PDMS, nanocomposite.

## I. INTRODUCTION

HIGH-AMPLITUDE, pulsed ultrasound has been considered as a versatile tool for noninvasive medical therapies, including sonothrombolysis, sonoporation, drug delivery, and lithotripsy [1]. Conventional piezoelectric materials have been mainly used to comprise high power ultrasound transducers in past decades [2]. In recent years, the photoacoustic mechanism has been investigated with increasing attention due to its broadband, high amplitude pulse-generation without electrical breakdown [3]–[6]. The conversion of laser pulse (pulse duration  $<10$  ns) into mechanical deformation through the thermoelastic interaction generates a wide-band ultrasound waves [3].

Manuscript received December 13, 2017; revised March 23, 2018 and May 3, 2018; accepted May 31, 2018. Date of publication June 8, 2018; date of current version September 6, 2018. This work was supported in part by the NC State Research Innovation Seed Funding under Grant #762162, in part by the, Natural Science Foundation of Chongqing under Grant cstc2017jcyjAX0188, and in part by the Fundamental Research Funds for the Central Universities under Grant 106112017 CDJQJ118846. The review of this paper was arranged by the IEEE NANO 2017 Guest Editors. (Corresponding author: Xiaoning Jiang.)

W.-Y. Chang, X. A. Zhang, J. Kim, A. Bagal, C.-H. Chang, T. Fang, and X. Jiang are with the Department of Mechanical and Aerospace Engineering, North Carolina State University, Raleigh, NC 27695 USA (e-mail: wchang5@ncsu.edu; xzhang27@ncsu.edu; jkim50@ncsu.edu; asbagal@ncsu.edu; cchang7@ncsu.edu; tfang2@ncsu.edu; xjiang5@ncsu.edu).

W. Huang is with the State Key Laboratory of Mechanical Transmission, Chongqing University, Chongqing 400044, China (e-mail: whuang@cqu.edu.cn).

H. F. Wu is with the Department of Energy, Vehicle Technologies Office, Energy Efficiency and Renewable Energy, Washington, DC 20585 USA (e-mail: felix.wu@ee.doe.gov).

Digital Object Identifier 10.1109/TNANO.2018.2845703

The advantages of high-frequency acoustic output ( $>10$  MHz), short pulse ( $<100$  ns) and broad bandwidth ( $\sim 6$  dB fractional bandwidth of  $>100\%$ ) have been highlighted in cell removal, drug delivery, and tissue incision applications [4], [7], [8]. The two main components of photoacoustic transmitter are a light absorption layer and a thermal expansion layer [9]. As a absorption layer, various types of nanostructures were exploited including thin metal films, two-dimensional gold nanostructure arrays, carbon nanotubes (CNT) and carbon nanofibers (CNF) [10]–[12]. For enhancing thermal expansion, polydimethylsiloxane (PDMS) has been usually selected as the interface between the light absorption layer and the external medium because of its excellent thermal expansion properties ( $0.92 \times 10^{-3} \text{ K}^{-1}$ ). As evidence, the nanocomposite transducer with a Cr/PDMS film exhibited approximately a 20 dB photoacoustic signal improvement compared to a Cr film-only photoacoustic transducer [10].

To date, the composite film transmitters made of carbon-based material and PDMS have shown its exceptional photoacoustic conversion efficiency (the ratio of the optical input to the acoustic energy output) compared to other homogeneous film materials [4], [12], [13]. Unique optical properties have been observed in CNT, such as photonic effects and high absorptivity [14]–[16]. For photoacoustic applications, the photoacoustic conversion efficiency of the CNT-PDMS composite is  $1.4 \times 10^{-3}$ , which is approximately a hundred times higher than other metal/PDMS composites [4]. Bao *et al.* used finite difference time domain (FDTD) simulations to analyze the relation between absorption, volume fraction, and thickness. [17]. The non-uniform, carbon black/PDMS mixture is even more efficient than the metal film/PDMS composite, which shows great potential in sonothrombolysis using a laser generated focused ultrasound transducer [9], [18].

Recently, candle soot nanoparticles (CSNP) have attracted increasing attention due to its simple synthesis process. Owing to the excellent electrical properties and branch-like nanostructures, candle soot (CS) has been used to build superhydrophobic surfaces, fabricate infrared sensors, and improve volumetric receivers [19]–[21]. More recently, we demonstrated that CSNP/PDMS composite is an effective photoacoustic transducer structure with a high photoacoustic efficiency ( $4.41 \times 10^{-3}$ ) [13].

Despite our initial success in CS/PDMS photoacoustic transducer demonstration, the transduction mechanism and the relationship between the CS structural property and the photoacoustic transduction efficiency have not been fully addressed

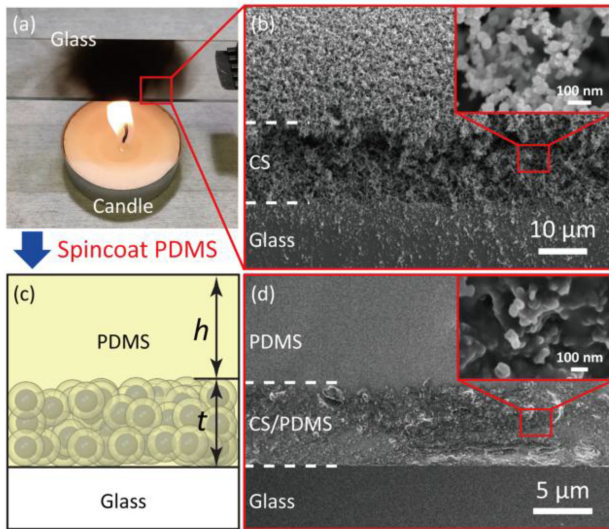


Fig. 1. (a) Photograph of candle soot deposition on a glass slide. (b) Scanning electron micrograph of the deposited candle soot film. The inset shows the interconnected carbon particle network. (c) Diagram of the candle soot/PDMS nano-composite after PDMS spin coating.  $h$  and  $t$  indicate the layer thicknesses of the upper PDMS and the CS/PDMS nano-composite, respectively. (d) Scanning electron micrograph of the candle soot/PDMS nano-composite with magnified view in the inset.

yet. In this paper, we demonstrate the effects of CS absorption layer structure and thickness on the photoacoustic transduction. This work is built upon our previous work [13] to clarify the dominant influence of CS structural conditions on highly-efficient photoacoustic transduction. We studied the contribution of light absorption property to the photoacoustic transduction of CS/PDMS nanocomposites. The constitutive materials were modeled with FDTD simulations and characterized using a spectrophotometer. The photoacoustic transduction efficiency was analyzed based on the characterized results.

## II. Methods

### A. Fabrication of CS/PDMS Nanocomposite

A flame synthesis using a paraffin wax candle flame was executed to generate carbon nanoparticles [19]. The overall fabrication procedure was modified from our previous work [13]. This modification was made for gaining more precise control of the CS layer deposition. The CS was deposited on a glass slide placed about 2 cm above the wick, resulting in a coated area of approximately 25 mm by 25 mm, as shown in Fig. 1(a). By changing the deposition time, different thicknesses of CS can be deposited. The cross section of a sample with a 30 sec CS deposition time is shown in Fig. 1(b). The diameter of each particle shown is  $40 \pm 5$  nm. When gas molecules collide against evaporated CS nanoparticles, CS nanoparticles lose their kinetic energy and form clusters [19]. The CS particles stick at the point of impact on the glass surface and then develop branch-like porous structures with mechanical stability [17], [21]. The mechanism is molecular diffusion, which depends on the ratio of the characteristic pore dimension ( $r_p$ ) and mean free path ( $\lambda$ ).

The branch-like structures can be predicted and simulated by Knudsen diffusivity calculations [22].

Meanwhile, a PDMS thermal expansion layer was fabricated. The PDMS was prepared with a base and curing agent (Sylgard 184) with a ratio of 10:1, and then degassed for 30 min in a vacuum chamber. For lowering viscosity of the uncured PDMS, toluene was added to the PDMS by a weight ratio of 1:100 (toluene: PDMS). Next, PDMS was spin-coated directly on the CS-coated glass slide to clear away extra PDMS, as well as control the thickness of the pure PDMS layer shown in Fig. 1(c). The CS/PDMS composite samples were later placed on a hot plate at  $65^\circ\text{C}$  for 1h (VWR, standard series  $7 \times 7$  hotplate, PA) to fully cure the PDMS and eliminate the added toluene. A cross section view of the laminar (PDMS, CS/PDMS, and glass layer) stack is shown in Fig. 1(d). Each CS nanoparticle was fully covered with PDMS, with an average inter-particle spacing of about 70 nm.

### B. Optical and Acoustic Measurements

The thicknesses of each constitutive layers were measured using a field emission scanning electron microscope (FE-SEM, FEI Verios 460L, OR). The measured thickness of PDMS and CS/PDMS composite layer on five different points were averaged. Light absorption properties of the CS/PDMS nanocomposites were measured. The absorption properties for the visible wavelength range were measured using a spectrophotometer and an integrating sphere (Agilent, Cary 5000, CA) at normal incidence at the samples with different CS/PDMS composite thicknesses. Total transmission,  $T$ , and reflection,  $R$ , of each sample were measured, and absorption was obtained as  $1-T-R$ .

The acoustic pressure output and bandwidth of prototyped transmitters were measured using the setup reported in our previous work [13]. We used the laser source of 532 nm wavelength Q-switched Nd:YAG pulse laser with a pulse duration of 6 ns and a repetition rate of 10 Hz (SL-III-10, Continuum, San Jose, CA). The calibrated hydrophone (HGL-0085, ONDA Crop., Sunnyvale, CA) was positioned 7.5 mm away from the transmitter radiation surface. The measurement location was in the near field region to acquire Gaussian pulse shape with less attenuated pressure amplitudes [23]. The detected shock wave signals were monitored and acquired using a digital oscilloscope (DSO7104B, Agilent, Santa Clara, CA). In this work, low laser energy (less than 1 mJ/pulse) was used for the following reason. In the low laser energy region, the output acoustic pressure is proportional to the input laser energy, as reported by Bacc *et al.* [4] and Chang *et al.* [13]. Hence, the low laser energy values from 0.3 mJ/pulse to 1 mJ/pulse with various absorption layer thicknesses were investigated.

### C. Optical Simulation

Light absorption properties of the CS/PDMS composites were simulated using Lumerical's FDTD Solutions 8.9. This simulation enabled an analysis of light absorption properties with different volume fractions of CSNPs. While computation speed for FDTD is limited by mesh size and simulation domain size,

the accuracy is comparable to analytical methods when mesh size is small. In addition, we regard FDTD technique as a complementary method to analytical method in that FDTD simulations can give more visual insights on light-matter interactions within the composites. We believe this information is helpful to further understand the mechanism of photoacoustic effect. In the simulation, the diameter of carbon nanoparticles was set uniformly to be 40 nm, as observed in the scanning electron micrographs. Since the inter-particle distance and particle diameter are roughly ten times smaller than the visible wavelengths, the distribution of the carbon particles was simplified to three-dimensional periodic square lattices in the simulation. The inter-particle distances were fixed at about 65 nm and 72 nm for carbon volume fractions of 12% and 9%, respectively. The simulation was conducted in three dimensions with periodic boundary conditions along  $x$  and  $y$  directions, and absorption boundary conditions in  $z$  direction. Mesh size is 4 nm in all three dimensions, which is 1/10 of the size of the carbon particle to ensure accuracy. The structures were directly illuminated by a pulsed light source for spectral analysis in the visible wavelength range. The PDMS volume was assumed to be non-dispersive with a constant refractive index of 1.41, and the refractive index of amorphous carbon was from the reference work [31]. For both experimental and numerical measurements, transmission spectra under unpolarized illuminations were calculated by averaging transverse-electric (TE) and transverse-magnetic (TM) results. To ensure numerical stability, FDTD Solutions uses a default stability factor value, which satisfies Courant's conditions. All the simulations in this work run successfully without instability detected by the software.

### III. RESULTS AND DISCUSSION

#### A. Characterization of CS/PDMS Composites

The fabricated CS/PDMS composite films were then characterized for a photoacoustic transduction study. The scanning electron micrographs of the CS/PDMS composite samples with 10 sec, 30 sec, and 120 sec CS deposition times are shown in Fig. 2(a)–(c). Based on the observation of sample cross section, a linear relationship between the thickness of the CS/PDMS layer ( $t$ ) and CS deposition time ( $\tau$ ) is shown in Fig. 2(d). The standard deviation of the CS/PDMS layer thickness for each sample is less than  $0.3 \mu\text{m}$ , which suggests that the thickness of the light absorption layer (CS/PDMS) can be effectively controlled under the deposition time control. The dashed line in Fig. 2(d) shows the thickness of the pure PDMS layer ( $h$ ) on different samples that were prepared with a spin speed of 3000 rpm, which is about  $16 \mu\text{m}$  (standard deviation is less than  $0.65 \mu\text{m}$ ). Previous work confirmed that the acoustic attenuation of the pure PDMS layer ( $<0.1 \text{ dB}/\mu\text{m}$  at 100 MHz) was negligible, and a PDMS layer greater than  $2 \mu\text{m}$  thickness was necessary to isolate light-induced-thermal waves from the water-composite interface [11]. Thus, we maintained the pure PDMS thickness ( $16 \mu\text{m}$ ) as a constant variable, and evaluated the effect of different thicknesses of CS/PDMS layers on the photoacoustic transduction performance.

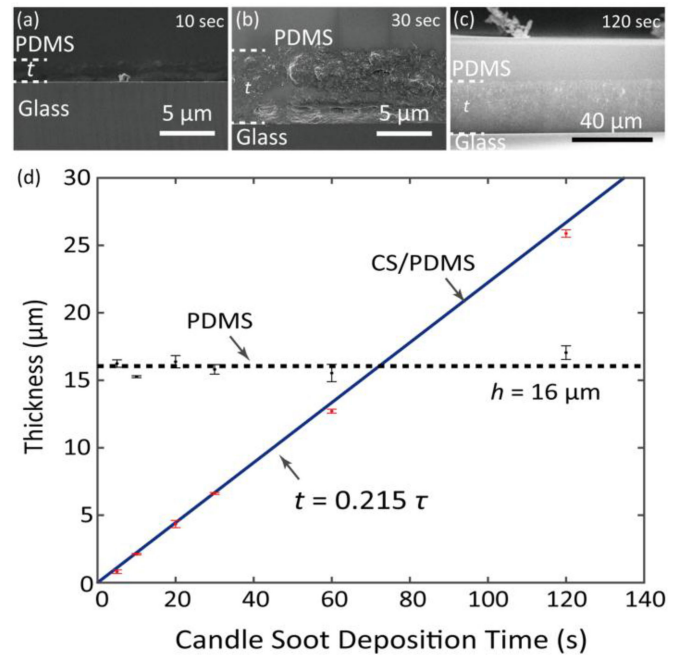


Fig. 2. (a)–(c) Scanning electron micrographs of the candle soot/PDMS nano-composites with CS deposition time of 10 sec, 30 sec and 120 sec, respectively. (d) Linear relationship between candle soot/PDMS nano-composite thickness,  $t$ , and the CS deposition time,  $\tau$ . The pure PDMS layer thickness remains constant.

The optical absorption measurement results were compared with the simulation results. The FDTD simulation model was shown in Fig. 3(a). The measured absorption spectra are shown in Fig. 3(b), where candle soot deposition time varies from 5 sec to 30 sec. It can be observed that higher absorption occurs with longer carbon deposition time due to longer absorption path length. For carbon deposition times longer than 120 sec, the composite becomes very absorptive and the absorption saturates at around 96% due to the Fresnel reflection from the flat glass/air interface. According to the reference for amorphous carbon refractive index [24], the percentage errors in their index data are 3.5% for refractive index, and 7% for extinction coefficient. For comparison between FDTD and experiments, the maximum percentage error is 2.6% in the results shown in Fig. 3(b). The absorption measurements for 20 sec, 60 sec and 120 sec CS/PDMS samples were performed using the spectrophotometer as described above. The data plot is shown in Fig. 3(c), where 60 sec and 120 sec samples show similar absorption near 96% while 20 sec sample exhibits lower absorption. The reflection could be mitigated by using anti-reflection coatings [20]–[22].

#### B. Optical Simulation Results

Commonly-used hexagonal and square lattices were used in FDTD simulations with same solid fraction of carbon. The absorption spectra for both lattice types are shown in Fig. 4. The absorption difference is also plotted. In terms of the periodic order type, it was found that the simulated absorptions from simple squares and hexagonal lattices with the same carbon volume fraction were not significantly different, both lattices

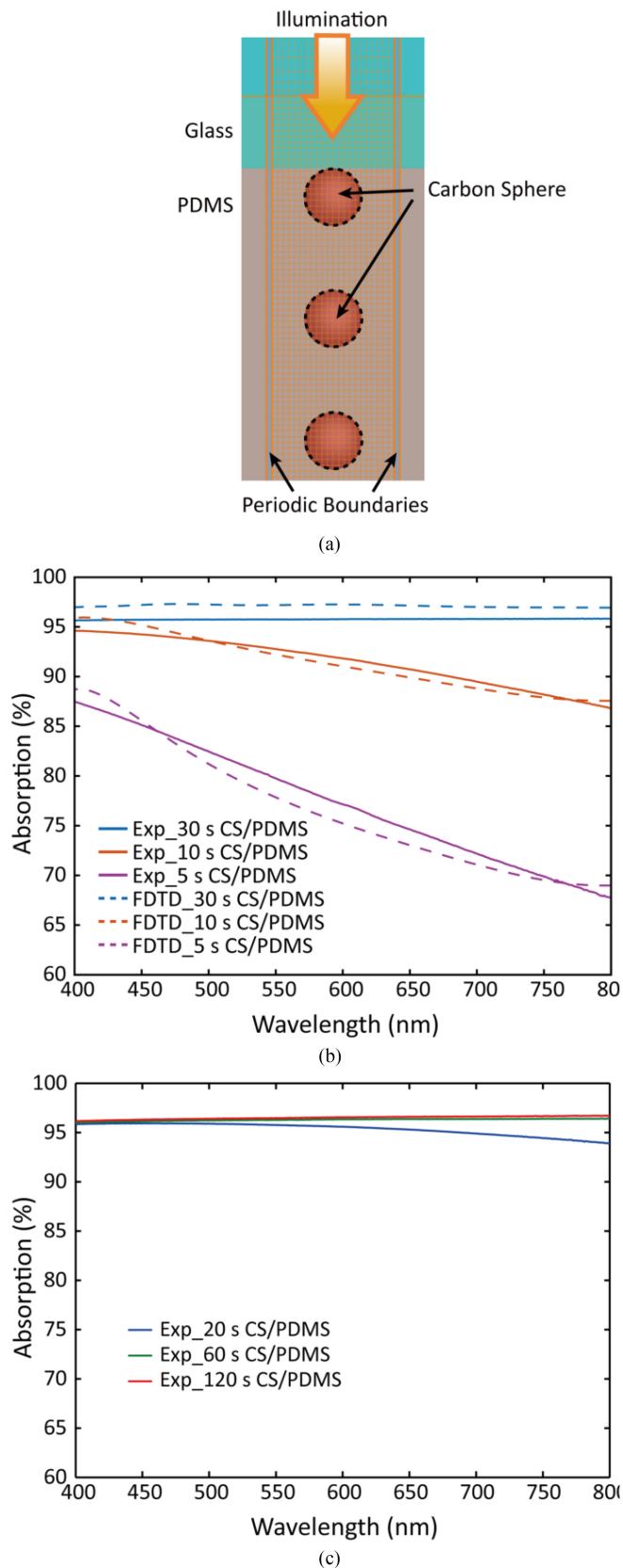


Fig. 3. (a) The FDTD simulation model. (b) Optical absorption measurement (solid lines) and FDTD simulation results (dashed lines) for candle soot/PDMS nano-composites with CS deposition time of 5 sec, 10 sec and 30 sec, respectively. (c) Measured absorption for 20 sec, 60 sec and 120 sec CS/PDMS nano-composites.

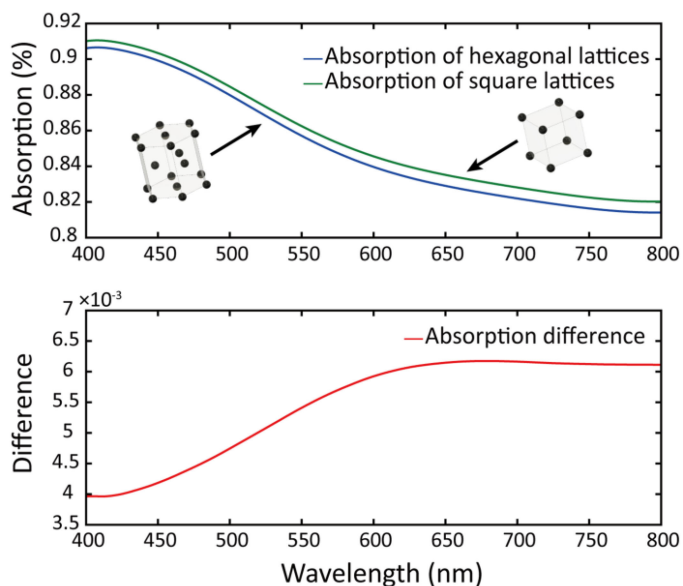


Fig. 4. Simulated absorption results between square and hexagonal lattices with the same carbon solid volume fraction. The absorption difference is about 0.006.

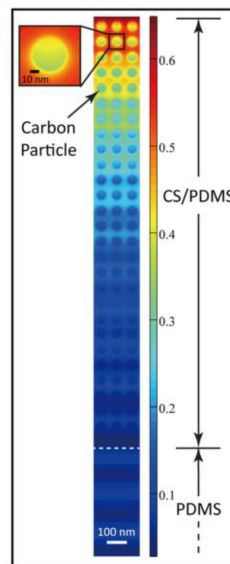


Fig. 5. Light intensity distribution within the candle soot/PDMS nano-composite with 10 sec CS deposition using FDTD simulation. Three-dimensional periodic square lattice is used for carbon particle configurations.

follow the same trend and the maximum absorption difference is about 0.006. Therefore, both lattices can be used to model the carbon composites without significant difference. For simplicity, square lattice was chosen in our FDTD modeling. From this observation, we anticipated that the solid volume fraction of the carbon particles would determine the absorption of the composite, while the carbon nanoparticle arrangement would play a less important role. The refractive index of the amorphous carbon was taken from previous work [24]. For the sample with a 10 sec carbon deposition time, the simulated light intensity distribution within the composite is depicted in Fig. 5, where a decaying intensity pattern along the thickness direction is observed. Similar

decaying intensity patterns are also found in other simulations with different carbon deposition time, but the decay lengths can vary. Here, we only show one simulated intensity map with 10 sec carbon deposition in Fig. 5 as an example. The structure in Fig. 5 shows actually three unit cells in the horizontal direction, for the purpose of better data presentation. Since we used square lattice for carbon particle arrangement, there is one carbon particle in one unit cell in horizontal direction.

To estimate the carbon volume fraction, the lattice constant of the square carbon lattice in the FDTD simulation was varied to fit the measurement results. Using this method, the estimated carbon volume fractions for the nano-composites with 5 sec and 10 sec candle soot depositions were about 12% and 9%, respectively. For samples with carbon deposition times longer than 10 sec, the above fitting method can no longer yield accurate results because the differences in light absorption for different high carbon volume fractions are so small that a small error in absorption measurement can lead to large error in volume fraction calculations. Therefore, the carbon volume fractions for samples with carbon deposition times longer than 10 sec were all assumed to be 9%, based on the assumption that the three-dimensional carbon nanoparticle arrangement would be more stable for longer deposition times, thus the carbon volume fraction would remain unchanged. However, at a 5 sec deposition time, the carbon structures could easily collapse during spin-coating, resulting in a larger volume fraction of about 12%. Although 5 sec deposition results in the higher volume fraction (12%) than >10 sec deposition cases (9%), a thin, porous layer of carbon particles (< 1  $\mu\text{m}$ ) absorb lower amount of light (<88%), whereas the thicker carbon layers (>2  $\mu\text{m}$ ) enable enhanced light absorption (>94%) despite the slightly lower volume fraction (9%). The FDTD simulations agree well with the experimental measurement for thicker samples, as shown for the sample with a 30 sec CS deposition time in Fig. 3(b). The wavelength-dependent absorption coefficients of the nanocomposites were calculated as well, using the Maxwell-Garnett effective medium approximation [28]. Due to the coherent light source in the simulation, a pattern as a result of interference can be observed along the thickness direction. Incoherence was considered when comparing absorption spectra between simulation and experiments using a Lorentzian spectral averaging method described in literature [29]. Maxwell-Garnett theory takes the following form, Eq. (1):

$$\frac{\varepsilon_{eff} - \varepsilon_{PDMS}}{\varepsilon_{eff} + 2\varepsilon_{PDMS}} = f \frac{\varepsilon_C - \varepsilon_{PDMS}}{\varepsilon_C + 2\varepsilon_{PDMS}} \quad (1)$$

where  $\varepsilon_{eff}$  is the effective dielectric constant for the CS/PDMS nanocomposite,  $\varepsilon_{PDMS}$  is PDMS dielectric constant,  $\varepsilon_C$  is the dielectric constant for amorphous carbon, and  $f$  is the carbon volume fraction. By solving the effective dielectric constant of the composite, the extinction coefficient,  $k$ , can be obtained by taking the imaginary part of the effective refractive index. The absorption coefficient,  $\alpha$ , is calculated by the following Eq. (2),

$$\alpha = \frac{4\pi}{\lambda} k \quad (2)$$

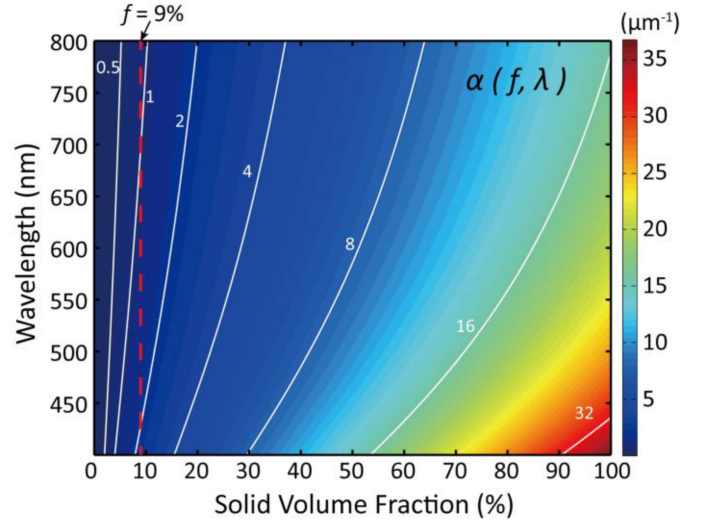


Fig. 6. Absorption coefficients calculated by Maxwell-Garnett theory as a function of carbon solid volume fraction and wavelength. Contours are plotted for absorption coefficients.

where  $\lambda$  is the wavelength. Fig. 6 illustrates that the absorption coefficient for CS/PDMS nanocomposite is between 0.9  $\mu\text{m}^{-1}$  and 2.3  $\mu\text{m}^{-1}$  for 9% carbon volume fractions within the visible wavelength range.

### C. Acoustic Pressure Output Measurement Results and Energy Conversion Efficiency Calculation

The photoacoustic transduction efficiency was determined by measuring the peak-to-peak pressure amplitudes. Fig. 7 shows acoustic output as a function of laser energy for CS/PDMS nanocomposites with CS deposition times longer than 5 sec. The results of CS/PDMS nanocomposites with 5 sec CS deposition times were separately analyzed, due to the unstable structure and different carbon volume fractions (12%) of the nanocomposites. The 5 sec CS/PDMS ( $t = 0.8 \mu\text{m}$ ) nanocomposite showed the lowest acoustic output due to its lack of absorption material. The 10 sec and 20 sec CS/PDMS ( $t = 2.2 \mu\text{m}$  and  $4.3 \mu\text{m}$ ) exhibit higher acoustic output pressure than the 5 sec CS/PDMS. On the other hand, as the thickness of CS/PDMS increases, extra CS/PDMS consumes most of the laser energy and high-frequency acoustic waves that have been attenuated in the extra CS/PDMS. Thus, the acoustic pressure decreases as the CS/PDMS layer increases in thickness, as shown in the results from the 60 sec and 120 sec CS/PDMS nanocomposite. Both positive and negative pressures showed highly linear relationships with laser energy for each sample in Fig. 7(a) and (b), which supports recent findings [30]. The -6 dB fractional bandwidth and peak pressure decrease when the thickness of the CS/PDMS layer increased. The waveforms and frequency spectra of photoacoustic transducers are shown in Fig. 8. The -6 dB frequency bandwidths of 10 sec, 30 sec and 120 sec CS/PDMS samples are 22.8 MHz, 22.6 MHz and 19 MHz, respectively. At a laser energy of 1 mJ/pulse, the peak pressure of a 10 sec CS/PDMS sample is as high as 3.78 MPa, and it is close to the output value of a focused optoacoustic transducer [4].

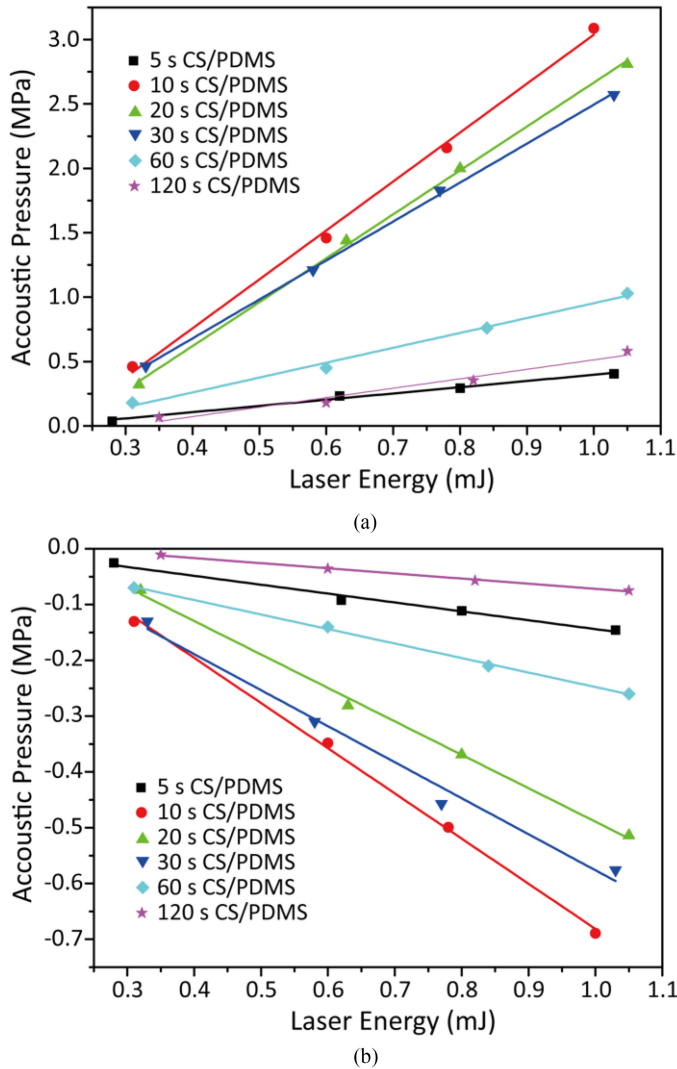


Fig. 7. The photoacoustic transduction measurements. (a) Peak positive pressure and (b) peak negative pressure output as a function of laser energy for three different CS/PDMS nano-composite samples: 5 sec CS/PDMS, 10 sec CS/PDMS, 20 sec CS/PDMS, 30 sec CS/PDMS, 60 sec CS/PDMS and 120 sec CS/PDMS.

This can be explained by the fact that the thermal elastic properties of thin layers outperform those of thicker layers when the light absorption of both layers is equal. The acoustic attenuation is negligible in pure PDMS film due to a lack of absorption material [10], [29]. In other words, when the thickness of the absorption layer (CS/PDMS layer) is greater than the optical absorption thickness, the output acoustic pressure increases as the thickness of the absorption layer decreases. As the composite thickness exceeds the optical absorption thickness, the majority of the light energy can be absorbed by the CS, becoming thermal energy. The thermal energy is finally transferred into PDMS to generate thermo-elastic expansion.

However, due to the large conductivity of CS and the branch-like structure, thermal energy can travel along the CS thickness simultaneously, resulting in a deeper heating domain in thicker

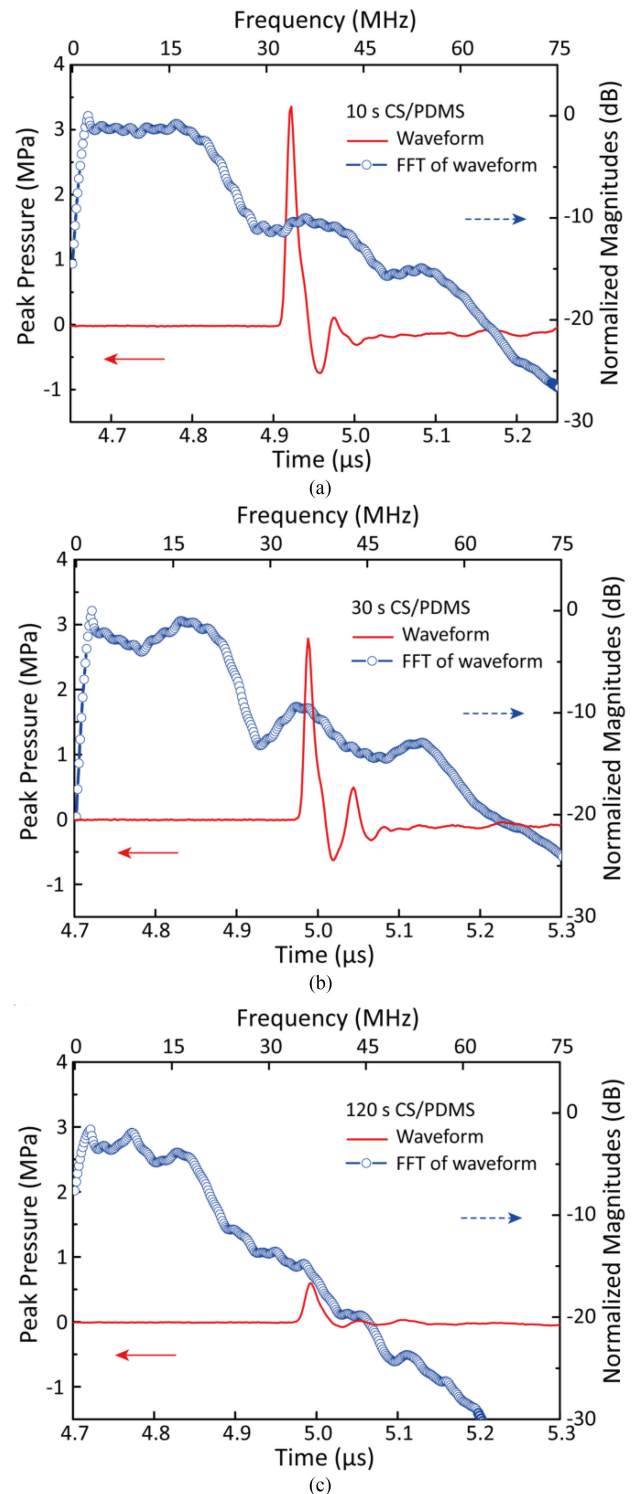


Fig. 8. The acoustic pressure and frequency spectra for different samples using a low laser input (1 mJ/pulse). (a) 10 sec CS/PDMS, (b) 30 sec CS/PDMS, and (c) 120 sec CS/PDMS.

CS/PDMS layers. Therefore, thermal energy is distributed more evenly in thicker layers than that in thinner layers, and therefore, lower acoustic pressure, given the identical total energy absorption. In addition, the observed acoustic wave has two

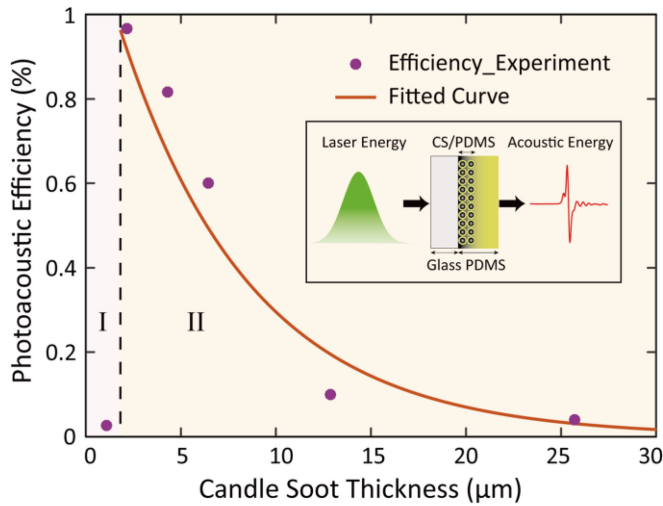


Fig. 9. The relationship between the photoacoustic transduction efficiency and the thickness of CS/PDMS nano-composites; the inset shows the schematic of photoacoustic effect.

parts. One is the forward traveling wave when PDMS is heated, and the other is the wave reflected by the glass substrate. The time delay between these two waves depends on the thickness of absorption layer, and is much shorter than the acoustic pulse duration over acoustic traveling depth [32]. These two waves interfere constructively, and shorter time delay between them results in higher acoustic output. In addition to acoustic pressure and bandwidth, photoacoustic efficiency, which is defined as Eq. (3) [13]

$$\eta = \frac{E_a}{E_{optical}} \quad (3)$$

is also important in a photoacoustic transduction evaluation. In the above equation,  $E_{optical}$  is the laser energy normalized with the actual absorbed laser energy in the layer, and  $E_a$  is the output of acoustic energy.  $E_a$  can be estimated by the following Eq. (4), assuming that the pressure was measured in water:

$$E_a = \frac{1}{\rho c} A \int_0^{\infty} p^2(t) dt \quad (4)$$

Where  $\rho$  is water density,  $c$  is sound velocity in water ( $\sim 1500$  m/s),  $p$  is the acoustic pressure measured by hydrophone, and  $A$  is the acoustic aperture area which can be considered as the same size of the laser beam in the near field. The normalized laser energy,  $E_{optical}$ , was measured by a pyroelectric energy sensor (J-50MB-YAG, Coherent, Portland, OR) and multiplied with the absorption of CS/PDMS composite. For the Gaussian pulse laser with a pulse energy of 1 mJ/pulse, the calculated photoacoustic transduction efficiency for CS/PDMS nanocomposites with different CS depositions can be found in Fig. 9. In region I, the photoacoustic efficiency of a CS/PDMS sample with a 5 sec CS deposition time is about  $2.1 \times 10^{-4}$ . This low efficiency is likely caused by the insufficient thickness of the absorption layer ( $\sim 0.8$  μm, too thin to absorb most laser energy). The measured absorption and reflection are about 80.8% and 3.5%, respectively, indicating that about 15.7% of the

laser energy passes through the CS/PDMS layer at a wavelength of 532 nm. In region II, the photoacoustic efficiency reaches its peak at a CS/PDMS composite thickness of 2.15 μm, suggesting an optimal photoacoustic transduction thickness may exist in a photoacoustic transduction structure. The photoacoustic efficiency exhibits a clear exponential decay profile when  $t$  increases. The photoacoustic efficiency is  $9.60 \times 10^{-4}$  and  $3.89 \times 10^{-4}$  for CS/PDMS thicknesses of 12.7 μm and 25.9 μm, respectively. We speculate that the occurrence of the highest photoacoustic efficiency at the thickness of 2.15 μm is due to the full absorption of the laser energy while the lowest acoustic attenuation compared to that in thicker samples. Compare to 5 sec CS/PDMS, the 10 sec CS/PDMS has thicker absorption layer which can absorb and transform more laser light to acoustic pressure. On the other hand, the 20 sec, 30 sec and 60 sec CS/PDMS should absorb more laser energy. However, the thicker absorption layer becomes the higher resistance of heat transfer. In other words, the 10 sec CS/PDMS shows more thermal expansion than other thickness of CS/PDMS. The measured photoacoustic transduction efficiency of  $9.02 \times 10^{-3}$  is 51% more than that of our previous work [13], about six times higher than 2.6 μm thickness of carbon nanotube composite [4], [11], and about 50 times higher than gold nanoparticles composite which is about 105 μm in thickness [33]. The comparisons are shown in Table I.

The superior performance of the CSNP/PDMS composite photoacoustic transducer is the result of the nano-scale spatial configurations, and the reason can be explained in two ways. The first explanation is that heat diffuses from CS particles into adjacent PDMS by the temporal temperature gradient. The CS/PDMS layer has a low interfacial thermal resistance thus a high rate at which heat releases into PDMS [13], [34]. The other explanation is based on the collectively-diffusive thermal effect, which explains the thermal properties of nanoparticles. Depending on the spacing between neighboring nanoparticles, the thermal transport may be significantly different. When the spacing of a neighboring heat source is small compared to the dominant mean free paths, the phonons originating from neighboring heat sources can interact with each other, resulting in a more efficient thermal diffusion [35]. In other words, nano scale heat sources cool faster when placed closer together, which is an effect that can explain the efficiency of the CS/PDMS absorption layer. The three-dimensional structures of ball-shaped CS particles are much more conductive for thermal energy releasing than two-dimensional and one-dimensional structures, such as carbon nanofibers or carbon nanotubes [5], [12]. Furthermore, PDMS, as a highly thermal elastic material, makes direct contact with the carbon nanoparticles to receive most of the heat energy generated from the three-dimensional nanostructures, resulting in low thermal transfer loss [36]. Herein an efficient photoacoustic conversion can be obtained. We also speculate that the small volume fraction of carbon nano-particles (9%) leaves a larger volume for PDMS (91%), which would allow for more thermal expansion. As a result of the efficient CS-PDMS thermal transfer and thermal expansion, high amplitude acoustic waves could then be generated.

TABLE I  
PHOTOACOUSTIC EFFICIENCY IN DIFFERENT MATERIAL

Material	Thickness of composite total thickness (absorption material thickness/PDMS thickness)	Laser power (mJ/cm <sup>2</sup> )	Photoacoustic efficiency	Reference
CNT/PDMS	2.6 μm (1.2 μm/1.4 μm)	42.4	$1.4 \times 10^{-3}$	[4], [11]
Gold-nanoparticle/PDMS	105 μm	8.75	$1.8 \times 10^{-4}$	[33]
Cr/PDMS	25 (100 nm/25 μm)	3.57	$8 \times 10^{-5}$	[13]
Carbon black/PDMS	30 μm	3.57	$3.4 \times 10^{-4}$	[13]
Carbon nanofiber/PDMS	57.8 μm (24.4 μm/33.4 μm)	3.57	$1.66 \times 10^{-3}$	[12], [13]
Candle soot/PDMS	25 μm (6 μm/19 μm)	3.57	$4.41 \times 10^{-3}$	[13]
Candle soot nano-composite/ PDMS	18 μm (2 μm/16 μm)	1	$9.02 \times 10^{-3}$	

#### IV. CONCLUSION

This study explores the relationship between the structural property and device performance of photoacoustic transducers by utilizing candle soot nanoparticle/PDMS nanocomposites. The optical absorption of CS/PDMS nanocomposites are up to 96% in the experiment. The optical interactions with the carbon nanoparticles in the composite are examined with FDTD simulations, which indicates that the solid volume fraction of carbon particles is a critical factor. At the same time, photoacoustic experiments show a promising relationship between linear output acoustic pressure and laser input, as long as the laser pulse energy is lower than 1 mJ/pulse. For samples with a CS deposition time longer than 10 sec, photoacoustic efficiency decays exponentially as the thickness of CS increases. At the laser pulse energy of 1 mJ/pulse, the measured maximum acoustic output pressure and efficiency are 3.78 MPa and  $9.69 \times 10^{-3}$ , respectively. These findings suggest that the design optimization of CSNP/PDMS composite photoacoustic transmitters can realize highly efficient laser-ultrasound patches for industrial and biomedical applications.

#### REFERENCES

- [1] J.-M. Escoffre and A. Bouakaz, *Therapeutic Ultrasound*. Berlin, Germany: Springer, 2015.
- [2] S. Zhang, F. Li, X. Jiang, J. Kim, J. Luo, and X. Geng, "Advantages and challenges of relaxor-PbTiO<sub>3</sub> ferroelectric crystals for electroacoustic transducers – A review," *Prog. Mater. Sci.*, vol. 68, pp. 1–66, Mar. 2015.
- [3] Y. Hou, J.-S. Kim, S. Ashkenazi, M. O'Donnell, and L. J. Guo, "Optical generation of high frequency ultrasound using two-dimensional gold nanostructure," *Appl. Phys. Lett.*, vol. 89, no. 9, Aug. 2006, Art. no. 093901.
- [4] H. W. Baac *et al.*, "Carbon-nanotube optoacoustic lens for focused ultrasound generation and high-precision targeted therapy," *Sci. Rep.*, vol. 2, Dec. 2012, Art. no. 989.
- [5] H. W. Baac, J. G. Ok, T. Lee, and L. J. Guo, "Nano-structural characteristics of carbon nanotube-polymer composite films for high-amplitude optoacoustic generation," *Nanoscale*, vol. 7, no. 34, pp. 14460–14468, Aug. 2015.
- [6] R. K. Poduval *et al.*, "Optical fiber ultrasound transmitter with electrospun carbon nanotube-polymer composite," *Appl. Phys. Lett.*, vol. 110, no. 22, May 2017, Art. no. 223701.
- [7] J. Di, J. Kim, Q. Hu, X. Jiang, and Z. Gu, "Spatiotemporal drug delivery using laser-generated-focused ultrasound system," *J. Controlled Release*, vol. 220, pt. B, pp. 592–599, Dec. 2015.
- [8] T. Lee, W. Luo, Q. Li, H. Demirci, and L. J. Guo, "Laser-induced focused ultrasound for cavitation treatment: Toward high-precision invisible sonic scalpel," *Small*, vol. 13, no. 38, Oct. 2017, Art. no. 1701555.
- [9] Y. Hou, S. Ashkenazi, S.-W. Huang, and M. O'Donnell, "Improvements in optical generation of high-frequency ultrasound," *IEEE Trans. Ultrason., Ferroelect., Freq. Control*, vol. 54, no. 3, pp. 682–686, Mar. 2007.
- [10] T. Buma, M. Spisar, and M. O'Donnell, "High-frequency ultrasound array element using thermoelastic expansion in an elastomeric film," *Appl. Phys. Lett.*, vol. 79, no. 4, pp. 548–550, Jul. 2001.
- [11] H. W. Baac *et al.*, "Carbon nanotube composite optoacoustic transmitters for strong and high frequency ultrasound generation," *Appl. Phys. Lett.*, vol. 97, no. 23, Dec. 2010, Art. no. 234104.
- [12] B.-Y. Hsieh, J. Kim, J. Zhu, S. Li, X. Zhang, and X. Jiang, "A laser ultrasound transducer using carbon nanofibers-polydimethylsiloxane composite thin film," *Appl. Phys. Lett.*, vol. 106, no. 2, Jan. 2015, Art. no. 021902.
- [13] W.-Y. Chang, W. Huang, J. Kim, S. Li, and X. Jiang, "Candle soot nanoparticles-polydimethylsiloxane composites for laser ultrasound transducers," *Appl. Phys. Lett.*, vol. 107, no. 16, Oct. 2015, Art. no. 161903.
- [14] G. L. Zhao, D. Bagayoko, and L. Yang, "Optical properties of aligned carbon nanotube mats for photonic applications," *J. Appl. Phys.*, vol. 99, no. 11, Jun. 2006, Art. no. 114311.
- [15] Z.-P. Yang, L. Ci, J. A. Bur, S.-Y. Lin, and P. M. Ajayan, "Experimental observation of an extremely dark material made by a low-density nanotube array," *Nano Lett.*, vol. 8, no. 2, pp. 446–451, Feb. 2008.
- [16] T. Xu, H. Shi, Y.-K. Wu, A. F. Kaplan, J. G. Ok, and L. J. Guo, "Structural colors: From plasmonic to carbon nanostructures," *Small*, vol. 7, no. 22, pp. 3128–3136, Nov. 2011.
- [17] H. Bao, X. Ruan, and T. S. Fisher, "Optical properties of ordered vertical arrays of multi-walled carbon nanotubes from FDTD simulations," *Opt. Express*, vol. 18, no. 6, pp. 6347–6359, Mar. 2010.
- [18] J. Kim *et al.*, "Laser-generated-focused ultrasound transducers for microbubble-mediated, dual-excitation sonothrombolysis," in *Proc. IEEE Int. Ultrason. Symp.*, 2016, pp. 1–4.
- [19] X. Deng, L. Mammen, H.-J. Butt, and D. Vollmer, "Candle soot as a template for a transparent robust superamphiphobic coating," *Science*, vol. 335, no. 6064, pp. 67–70, Jan. 2012.
- [20] L. Yuan *et al.*, "Self-cleaning flexible infrared nanosensor based on carbon nanoparticles," *ACS Nano*, vol. 5, no. 5, pp. 4007–4013, May 2011.
- [21] G. Ni *et al.*, "Volumetric solar heating of nanofluids for direct vapor generation," *Nano Energy*, vol. 17, pp. 290–301, Oct. 2015.
- [22] S. C. Reyes and E. Iglesia, "Effective diffusivities in catalyst pellets: New model porous structures and transport simulation techniques," *J. Catalysis*, vol. 129, no. 2, pp. 457–472, Jun. 1991.
- [23] W. Huang, W. Y. Chang, J. Kim, S. Li, S. Huang, and X. Jiang, "A novel laser ultrasound transducer using candle soot carbon nanoparticles," *IEEE Trans. Nanotechnol.*, vol. 15, no. 3, pp. 395–401, May 2016.
- [24] C.-H. Chang, J. A. Dominguez-Caballero, H. J. Choi, and G. Barbastathis, "Nanostructured gradient-index antireflection diffractive optics," *Opt. Lett.*, vol. 36, no. 12, pp. 2354–2356, Jun. 2011.
- [25] S. Chattopadhyay, Y. F. Huang, Y. J. Jen, A. Ganguly, K. H. Chen, and L. C. Chen, "Anti-reflecting and photonic nanostructures," *Mater. Sci. Eng. R Rep.*, vol. 69, nos. 1–3, pp. 1–35, Jun. 2010.
- [26] K.-C. Park, H. J. Choi, C.-H. Chang, R. E. Cohen, G. H. McKinley, and G. Barbastathis, "Nanotextured silica surfaces with robust superhydrophobicity and omnidirectional broadband supertransmissivity," *ACS Nano*, vol. 6, no. 5, pp. 3789–3799, May 2012.
- [27] B. J. Stagg and T. T. Charalampopoulos, "Refractive indices of pyrolytic graphite, amorphous carbon, and flame soot in the temperature range 25° to 600 °C," *Combustion Flame*, vol. 94, no. 4, pp. 381–396, Sep. 1993.

- [28] P. Sarafis and A. G. Nassiopoulou, "Dielectric properties of porous silicon for use as a substrate for the on-chip integration of millimeter-wave devices in the frequency range 140 to 210 GHz," *Nanoscale Res. Lett.*, vol. 9, no. 1, pp. 1–8, Aug. 2014.
- [29] A. Bagal *et al.*, "Multifunctional nano-accordion structures for stretchable transparent conductors," *Mater. Horizons*, vol. 2, no. 5, pp. 486–494, 2015.
- [30] T. Lee, J. G. Ok, L. J. Guo, and H. W. Baac, "Low f-number photoacoustic lens for tight ultrasonic focusing and free-field micro-cavitation in water," *Appl. Phys. Lett.*, vol. 108, no. 10, Mar. 2016, Art. no. 104102.
- [31] W. Huang, W. Y. Chang, J. Kim, S. Li, S. Huang, and X. Jiang, "A novel laser ultrasound transducer using candle soot carbon nanoparticles," *IEEE Trans. Nanotechnol.*, vol. 15, no. 3, pp. 395–401, May 2016.
- [32] T. Lee, Q. Li, and L. J. Guo, "Out-coupling of longitudinal photoacoustic pulses by mitigating the phase cancellation," *Sci. Rep.*, vol. 6, Feb. 2016, Art. no. 21511.
- [33] X. Zou, N. Wu, Y. Tian, and X. Wang, "Broadband miniature fiber optic ultrasound generator," *Opt. Express*, vol. 22, no. 15, pp. 18119–18127, Jul. 2014.
- [34] Y.-S. Chen, W. Frey, S. Kim, P. Kruijinga, K. Homan, and S. Emelianov, "Silica-coated gold nanorods as photoacoustic signal nanoamplifiers," *Nano Lett.*, vol. 11, no. 2, pp. 348–354, Feb. 2011.
- [35] K. M. Hoogeboom-Pot *et al.*, "A new regime of nanoscale thermal transport: Collective diffusion increases dissipation efficiency," *Proc. Nat. Acad. Sci.*, vol. 112, no. 16, pp. 4846–4851, Apr. 2015.
- [36] R. J. Warzoha and A. S. Fleischer, "Heat flow at nanoparticle interfaces," *Nano Energy*, vol. 6, pp. 137–158, May 2014.

Authors' photographs and biographies not available at the time of publication.